ACS APPLIED ENERGY MATERIALS

www.acsaem.org

Article

Synthesis of Ni-Rich Layered-Oxide Nanomaterials with Enhanced Li-Ion Diffusion Pathways as High-Rate Cathodes for Li-Ion Batteries

Ming Jiang, Qian Zhang,* Xiaochao Wu, Zhiqiang Chen, Dmitri L. Danilov, Rüdiger-A. Eichel, and Peter H. L. Notten*

Cite This: *ACS Appl. Energy Mater.* 2020, 3, 6583−6590

Read Online

ACCESS | Metrics & More | Article Recommendations | Supporting Information

ABSTRACT: Ni-rich $LiNi_{0.6}Co_{0.2}Mn_{0.2}O_2$ nanomaterials with a high percentage of exposed {010} facets have been prepared by surfactant-assisted hydrothermal synthesis followed by solid-state reaction. Characterization by X-ray diffraction (XRD) and high-resolution transmission electron microscopy (HRTEM) confirmed that the particles have enhanced the growth of nanocrystal planes in favor of Li-ion diffusion. Electrochemical tests show these cathode materials endow a large Li-ion diffusion coefficient, which leads to a superior rate capability and cyclability, suggesting these cathode materials are highly beneficial for practical application in Li-ion batteries.

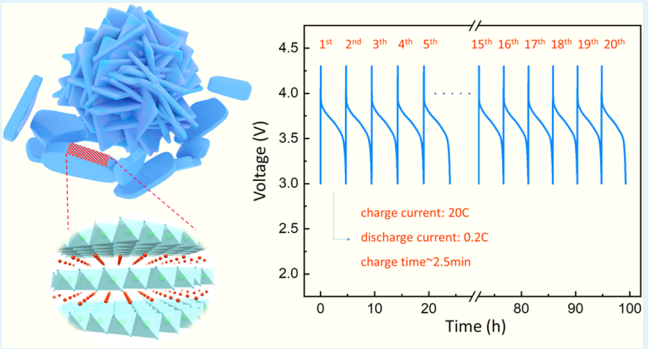

KEYWORDS: *Ni-rich cathodes, lithium-ion batteries, nanobrick structure, active facets, high rate*

1. INTRODUCTION

During the past decades, lithium-ion batteries (LIB) have been intensively studied as one of the most promising candidates for complementing fossil fuels in the energy storage field.[1−3] Up to now, LIB have successfully powered numerous electronic devices in practical applications, not only portable devices such as laptops, mobile phones, and cameras but also large-scale appliances such as electric vehicles (EV).[4,5] Smart grid systems are also considered as a potential market for LIB, as these batteries can cater to the needs of load balancing, uninterrupted power supply, and peak leveling at low cost.

To be compatible with the ever-growing industrial applications, there exists a high demand to pursue batteries with larger storage capacity, extended cycling performance, and better safety for future generations of energy storage.[6] Compared with the anode side, which can easily achieve a specific capacity of 4200 mAh g^{-1} (Si),[7,8] 994 mAh g^{-1} (Sn),[9] or 782 mAh g^{-1} (SnO_2),[10] optimization of the cathode side is always the bottleneck in LIB studies. Among the various cathode materials, Ni-rich layered transition-metal mixed-oxide $LiNi_xCo_yMn_{1-x-y}O_2$ (NCM, $x > 0.5$) has drawn intense attention in investigating high energy density, low cost, and reduced Co content cathode materials.[11,12] Within the class of Ni-rich cathode materials, $LiNi_{0.6}Co_{0.2}Mn_{0.2}O_2$ displays a better Li-ion diffusion behavior with negligible temperature dependence as well as an optimal balance between high energy density and cost efficiency.[13−15] However, despite the above merits, as the member of Ni-rich NCM cathodes, $LiNi_{0.6}Co_{0.2}Mn_{0.2}O_2$ is still suffering from several drawbacks. Further improvements and optimization are therefore necessary to utilize its full potential as next generation of cathode materials in LIB.

It has been established that cation disorder and volume expansion during Li-ion (de)intercalation are mainly responsible for the intrinsically poor rate capacity and moderate cycling stability of Ni-rich NCM cathodes.[16,17] Conventional NCM materials have a morphology with microsized, spherelike structure, in which crystal facets are randomly oriented and densely aggregated. Because of this disordered orientation, the intergrain stress, which mainly occurs at the grain boundaries, will be deteriorated along with volume expansion, which may provoke the development of cracks and eventually lead to inferior electrochemical performance.[18] Several strategies have been employed to overcome these problems, such as cation doping,[19,20] surface coating,[21−23] and structure modification.[24] However, cation doping and surface coating are always at the expense of energy density, as the introduced compounds are typically electrochemically inactive.[25] As the NCM material properties are strongly dependent on the microstructure, it has been identified that architecture control is crucial for promoting Li-ion transport within the electrodes, thereby

Received: April 6, 2020
Accepted: May 27, 2020
Published: May 27, 2020

https://dx.doi.org/10.1021/acsaem.0c00765
ACS Appl. Energy Mater. 2020, 3, 6583−6590

improving the electrode performance without compromising the energy density of NCM cathodes.

Ni-rich NCM cathode materials have a layered hexagonal structure with *R*3*m* space group. The Li-ion diffusion channels are oriented two-dimensionally, parallel to the Li layers along the *a*- and *b*-axes. Hence, in the hexagonal crystal, Li-ion diffusion active facets are denoted by {010}, consisting of (010), (0$\bar{1}$0), (100), (110), (1$\bar{1}$0), and ($\bar{1}$00) facets. The (001) and (00$\bar{1}$) facets, perpendicular to the *c*-axis, are closely packed by MO_6 (M = Ni, Co, Mn) octahedra, which hinder Li-ion transport and can therefore be considered as inactive Li-ion diffusion facets.[26−29] Based on the understanding of the NCM crystal structure, the efforts of structure modification are generally aiming at the fabrication of high-ratio {010} facets exposed materials. However, this is difficult to achieve as the NCM nanomaterials are dominated by {001} facets. This is related to the much lower surface energy of {001} facets, while the {010} facets are easily vanished during the synthesis process. Although various surfactants, such as polyvinylpyrrolidone (PVP)[30,31] and sodium dodecyl sulfate (SDS),[32] have been applied to synthesize favorable NCM crystals,[33] it still remains a challenge to structurally and morphologically control the growth conditions.

Herein, we designed and successfully synthesized Ni-rich $LiNi_{0.6}Co_{0.2}Mn_{0.2}O_2$ nanomaterials with a unique nanobrick NCM morphology (NB-NCM), which endows a significantly exposed ratio of high-energy {010} facets. A facile hydrothermal method was used in the synthesis, and a new type of surface-active agent cetyltrimethylammonium bromide (CTAB) has been introduced to control the particle growth. TEM measurements showed that the lateral surfaces of NB-NCM are active {010} facets. These highly exposed {010} facets accordingly resulted in favorable Li-ion diffusion coefficients. Consequently, the NB-NCM electrode materials demonstrated an enhanced rate capability, higher cycling stability, and fast charging characteristics compared to commercial NCM cathode materials. In addition, ordered structural orientation in NB-NCM microparticles displayed crack-free surfaces even after long-term cycling due to the moderate inner-grain stress induced by volume expansion.

2. EXPERIMENTAL SECTION

2.1. Material Synthesis. Synthesis of transition metal (TM) hydroxide precursor: the precursor was prepared by a hydrothermal method. Typically, 0.1 M TM-acetate (molar ratio of $Ni(CH_3COO)_2 \cdot 4H_2O$, $Mn(CH_3COO)_2 \cdot 4H_2O$, and $Co(CH_3COO)_2$ is 6:2:2), 0.2 M urea, and 0.1 M CTAB were evenly stirred in a mixed solution of deionized water and ethanol (volume ratio 1:1). After vigorous stirring, the reactant solution was transferred into the Teflon-lined stainless-steel autoclave. The autoclave was sealed and maintained in an oven at 150 °C for 5 h. After the reaction had been completed, the precipitate was washed and centrifuged three times by deionized water and dried overnight in an oven at 80 °C.

Synthesis of NB-NCM material: the as-prepared TM hydroxide precursor was thoroughly mixed with $LiOH \cdot H_2O$ in an agate mortar and calcinated at 500 °C for 4 h and at 750 °C for 10 h in air. Commercial $LiNi_{0.6}Co_{0.2}Mn_{0.2}$ (C-NCM), used as reference material, was obtained from Tianjin B&M Science and Technology Co., Ltd., China.

2.2. Material Characterization. Scanning electron microscopy (SEM) images were taken on a Quanta FEG 650 (FEI, USA) environmental scanning electron microscope operated at a voltage of 20 kV. X-ray diffraction (XRD) measurements were performed between 10° and 80° using Cu Kα radiation using an EMPYREAN X-ray diffractometer (Panalytical, Netherlands). The collected XRD intensity data were analyzed by FullProf Suite refinement software. Standard data of $LiNiO_2$ (ICSD_153550) and the "Profile Matching" configuration were applied in the analyses. Transmission electron microscopy (TEM), high-resolution transmission electron microscopy (HRTEM), and selected area electron diffraction (SAED) measurements were performed by using a Tecnai F20 (FEI) transmission electron microscope at an acceleration voltage of 200 kV. X-ray photoelectron spectroscopy (XPS) is performed by an Thermo Scientific K-Alpha instrument with a monochromatic X-ray source (Al Kα).

2.3. Electrochemical Measurements. The electrochemical performance was tested in Swagelok cells. The electrode slurry was a mixture of the active electrode materials, carbon black (Super P, Alfa Aesar), and poly(vinylidene fluoride) binder (PVDF, Sigma-Aldrich) at the weight ratio of 8:1:1. The mixture was then dissolved in *N*-methylpyrrolidone (NMP) solvent. The slurry was uniformly coated onto an aluminum foil, dried overnight at 90 °C, and then cut into discs of 12 mm diameter. Metallic lithium metal was used as both counter and reference electrode. 1 M $LiPF_6$ in a 1:1 mixed solvent of ethylene carbonate (EC)/dimethylcarbonate (DMC) LP30, BASF, USA) was used as electrolyte.

All electrochemical tests were performed in an MKF120 climate chamber (Binder, Germany) by using a VMP3 potentiostat (Bio-Logic, France). Galvanostatic charge/discharge cycling was operated in the voltage range of 3.0−4.3 V vs Li^+/Li. Cyclic voltammogram (CV) tests were operated in a voltage window of 3.0−4.3 V vs Li^+/Li at a scan rate of 0.1 mV s^{-1}. Electrochemical impedance spectroscopy (EIS) tests were conducted with an amplitude of 10 mV in the frequency range of 10−100 kHz. Galvanostatic intermittent titration (GITT) measurements were performed by using a small current of 0.05 C. The duration of each current pulse was 15 min and was followed by a 60 min resting period.

3. RESULTS AND DISCUSSION

The TM hydroxide precursor and NB-NCM material are schematically shown in Figure 1a. The precursor with nanoplate morphology serves as a skeleton in the subsequent calcination process. The porous morphology with three-dimensional widely opened pathways promotes Li-ion (de)-intercalation during the high-temperature solid-state reaction. The final NB-NCM product with exposed {010} facets maintained the original crystal structure for the Ni-rich cathode as indicated in Figure 1a. The morphologies of the TM hydroxide precursor and NB-NCM are shown in the scanning electron microscope (SEM) images of Figure 1b,c and Figure S1. Because of the adsorbate-directed reaction nature of the cationic surfactant CTAB, the precursors adopted the nanoplate architecture with an average diameter of around 1 μm and assembled randomly into a spherelike morphology.[34]

The CTAB molecules can effectively stabilize the surface energy of high-energy facets and guarantee the exposure of significantly increased number of {010} facets. After the lithiation reaction, the final NB-NCM product maintained a nanoplate architecture similar to that of the precursor. The as-grown nanobricks possess smooth surfaces and enhanced sidewalls. The thickness of these nanobricks is about 100 nm, which provides a high number of exposed {010} facets in contrast to commercial C-NCM materials with irregularly oriented particles (Figure S2). Upon comparison of Figures 1b and 1c, it is worthwhile to note that the thickness of the final product had increased significantly after the calcination process, which might be due to multilayer plate merging during the high-temperature reaction. The optimized structure provides not only fast Li-ion-transfer pathways during the (dis)charging process but also effective electrolyte penetration into the porous electrodes and, in addition, reduces the grain

https://dx.doi.org/10.1021/acsaem.0c00765
ACS Appl. Energy Mater. 2020, 3, 6583−6590

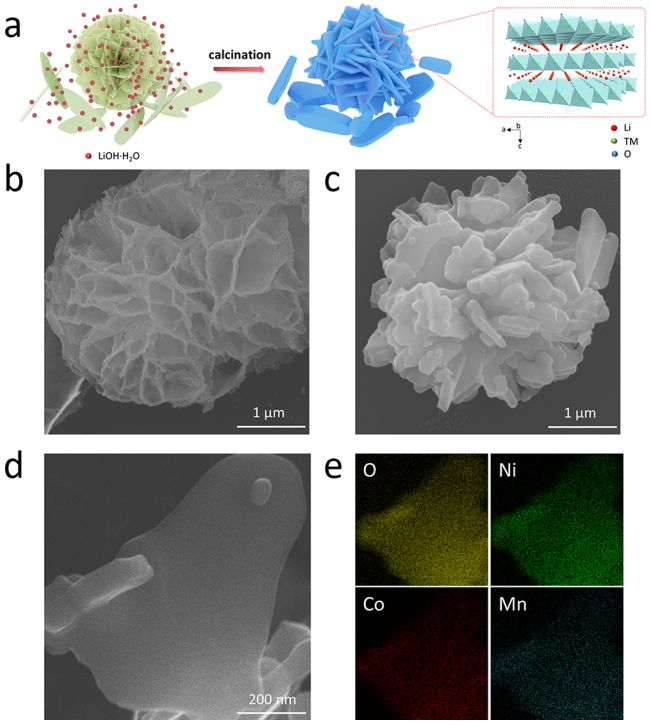

Figure 1. (a) Schematic representation of the TM hydroxide precursor and NB-NCM after calcination. SEM images of (b) the TM hydroxide precursor and (c) the NB-NCM product. (d) Magnified SEM image of a single NCM nanobrick. (e) EDS element mapping of a single nanobrick.

stress between the electrode particles during the (de)lithiation process. Figure 1d,e shows an example of element mapping results within a single NB-NCM particle. It is found that the Ni, Co, and Mn atoms are uniformly distributed. Energy-dispersive X-ray spectroscopy (EDS) reveals that the ratio of the metal atoms is 42.6:12.7:12.3, which is close to the designed metal precursor proportions (Figure S3).

Structural characterization of TM hydroxide precursor and NB-NCM has been performed by X-ray powder diffraction (XRD) and are shown in Figure S4 and Figure 2a, respectively. The peaks in the XRD patterns for TM hydroxide precursor can be assigned to typical $M(OH)_2$ compounds where M refers to Ni, Co, or Mn (Figure S4). Figure 2a confirms the high crystallinity of NB-NCM as it does not reveal any impurities. All diffraction peaks can be precisely indexed with an α-$NaFeO_2$ layered structure with $R3m$ space group. The distinctly separated peaks (003)/(104) and (110)/(018) indicate their well-crystallized layered structure. According to the calculated results, the intensity ratio of (003)/(104) of NB-NCM from the refined pattern is about 1.74, which is higher than that of the commercial C-NCM material (1.53 in Figure S5), implying the negligible cation mixing disorder.[16] Additionally, NB-NCM shows a slightly higher intensity ratio of 1.12 for (110)/(018) compared to C-NCM. These results exhibit the enhanced growth of {010} facets in NB-NCM, which must be attributed to the surfactant-assisted synthesis. The lattice parameters of NB-NCM and C-NCM as obtained from the Rietveld refinements are listed in Table S1 of the Supporting Information. The similar parameter values suggest that the synthetic optimization has only little effect on the materials lattice structure and that the real difference is related to the materials morphology.

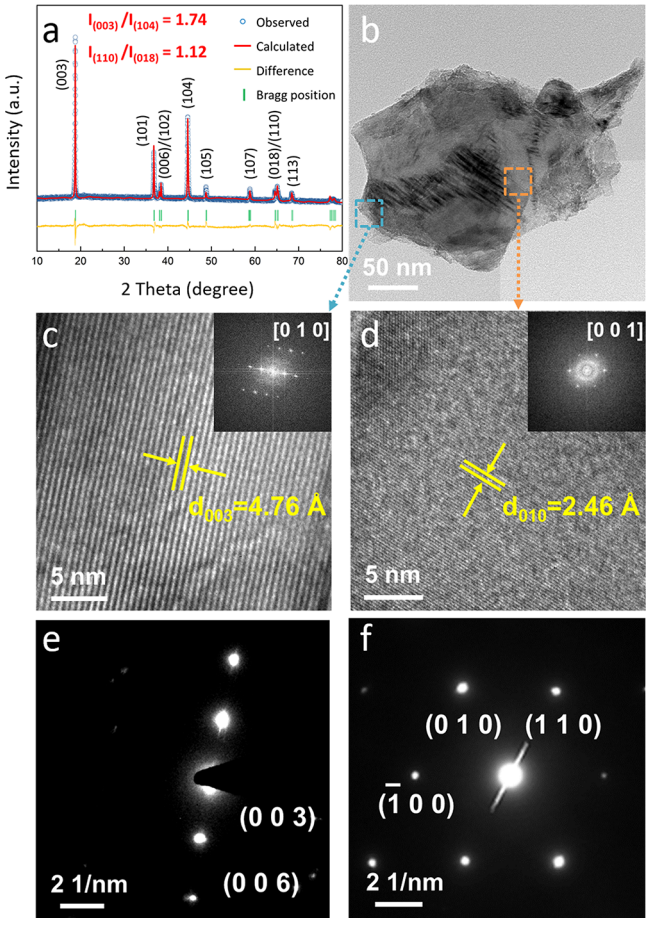

Figure 2. (a) Refined XRD patterns of NB-NCM. (b) TEM image of a single NB-NCM nanosheet. (c) HRTEM image of a lateral panel and (e) corresponding SAED pattern. (d) HRTEM image of a front panel and (f) corresponding SAED pattern.

To elucidate more detailed crystalline information about NB-NCM, TEM, HRTEM, and SAED studies were performed of an individual nanosheet (Figure 2). Figures 2c and 2d represent the HRTEM images of a lateral and front panel of a nanosheet, respectively. The observed apparent lattice fringes with interplanar spacings of 4.76 and 2.46 Å can be assigned to the (003) and (010) planes, respectively, suggesting that the nanosheets were growing along the *c*-axis. Combined with the SAED patterns, shown in Figure 2e,f, it can be concluded that the obtained NB-NCM nanosheets consisted of a (001) front panel and a (010) plane exposed on the lateral panel. Conclusively, these layered-structured cathode materials reveal two-dimensional Li-ion diffusion pathways perpendicular to the (010) plane, and this might favorably enhance the rate capability and power density of NB-NCM cathodes.[28,30,31,33,35,36]

X-ray photoelectron spectroscopy (XPS) has been performed on both NB-NCM and C-NCM to analyze the oxidation states of the chemical elements at the surface of the nanosheets. Figure 3a shows that Ni presents a mixture of two valence states for Ni^{2+} and Ni^{3+}. The peaks at 854.3 and 860.8 eV can be attributed to Ni^{2+} ($2p_{3/2}$) and Ni^{2+} ($2p_{1/2}$), respectively, while that located at 855.9 eV relates to Ni^{3+} ($2p_{1/2}$).[37] Interestingly, NB-NCM shows a relatively higher Ni^{2+} ratio in comparison with the C-NCM sample. According to previous studies, a NCM cathode material tends to be

https://dx.doi.org/10.1021/acsaem.0c00765
ACS Appl. Energy Mater. 2020, 3, 6583−6590

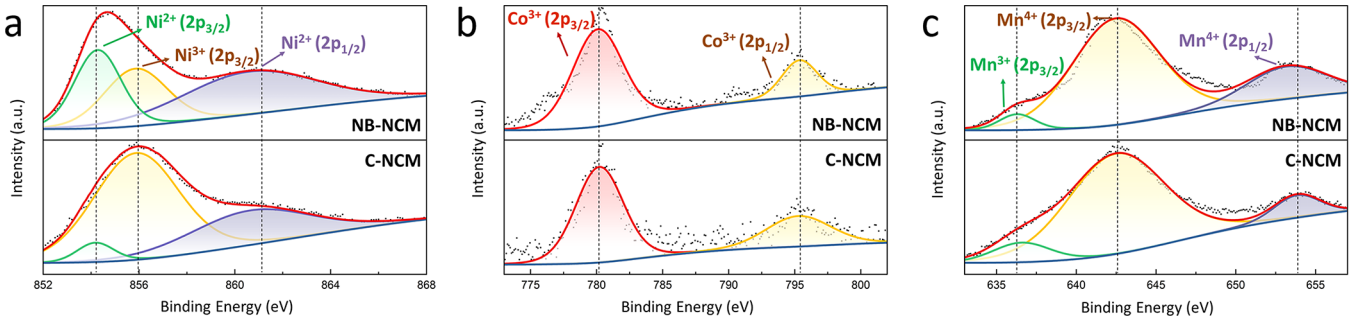

Figure 3. XPS spectra of (a) Ni 2p, (b) Co 2p, and (c) Mn 2p in as-prepared NB-NCM (upper curves) and C-NCM (lower curves).

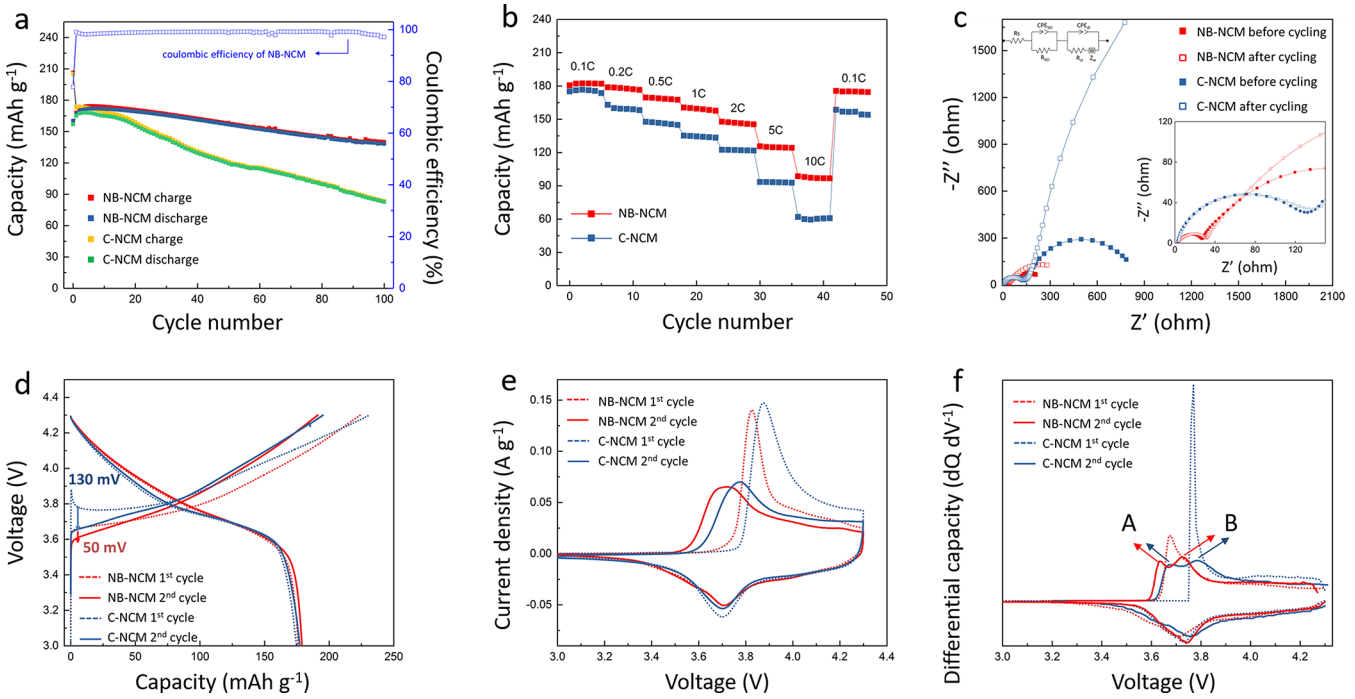

Figure 4. (a) Cycling performance of NB-NCM and C-NCM electrodes at 1 C rate. (b) Rate capability at various indicated C-rates. (c) EIS plots of both fresh and cycled electrodes (inset are zoom-in plots in the high-frequency region and analyzed equivalent circuit). (d) Constant current voltage (dis)charge curves in the first and second cycle. (e) CV curves of the first and second cycle at a scan rate of 0.1 mV s^{-1}. (f) Differential capacity curves of the constant current curves of (d) in the first and second cycle.

structurally more stable at higher Ni^{2+} content at the surface.[38] Figure 3b reveals the XPS spectra of Co 2p, where the peaks at 780.2 and 795.4 eV correspond to Co^{3+} ($2p_{3/2}$) and Co^{3+} ($2p_{1/2}$), respectively, implying that the most dominant cobalt oxidation state is Co^{3+}.[39] Additionally, the Mn 2p spectra indicate a mixture of Mn^{3+} and Mn^{4+} in both NB-NCM and C-NCM (Figure 3c).[40] In conclusion, these XPS results show almost identical valence states for NB-NCM and C-NCM, except for the Ni spectra: NB-NCM shows that the surface is enriched with Ni^{2+}, which might contribute to the better stability of these electrodes as will be shown below.

The electrochemical performance of both the NB-NCM and C-NCM material has been investigated to evaluate the structural advantages of NB-NCM to be applied as cathode material in LIB. Figure 4a shows the cycling stability of NB-NCM and C-NCM electrodes in the voltage range of 3.0−4.3 V at 1 C rate (1 C = 200 mA g^{-1}). Both samples were charged with a constant current up to 4.3 V followed by a constant voltage period of 30 min. The discharge was performed with a constant current. The mass loadings for both samples were the same, around 2 mg cm^{-2}. A sharp capacity drop occurs for both electrodes during the first cycle due to the activation process, resulting from the Li(OH) residue formed during the synthesis. After activation, the NB-NCM electrode combines a high initial capacity of 161 mAh g^{-1} with a high capacity retention of 86.9% after 100 cycles (141 mAh g^{-1}). The Coulombic efficiency maintains close to 100%. In comparison, the C-NCM electrode delivers a comparable initial storage capacity of 156 mAh g^{-1}, but the capacity degrades much faster. This distinct contrast between the two electrodes indicates that the cathode with an ordered oriented architecture is more stable upon cycling.

The rate capability is another limiting factor highly relevant for practical use in LIB. Figure 4b shows the influence of the current (0.1, 0.2, 0.5, 1, 2, 5, and 10 C) on the electrode storage capacity. The initial storage capacity of 180.6 mAh g^{-1} for the NB-NCM electrode at 0.1 C is reduced to 98.6 mAh g^{-1} at 10 C rate but can almost be fully recovered to 175.5 mAh g^{-1} at 0.1 C after 50 cycles, which shows a significantly better rate capability compared to that of C-NCM.

https://dx.doi.org/10.1021/acsaem.0c00765
ACS Appl. Energy Mater. 2020, 3, 6583−6590

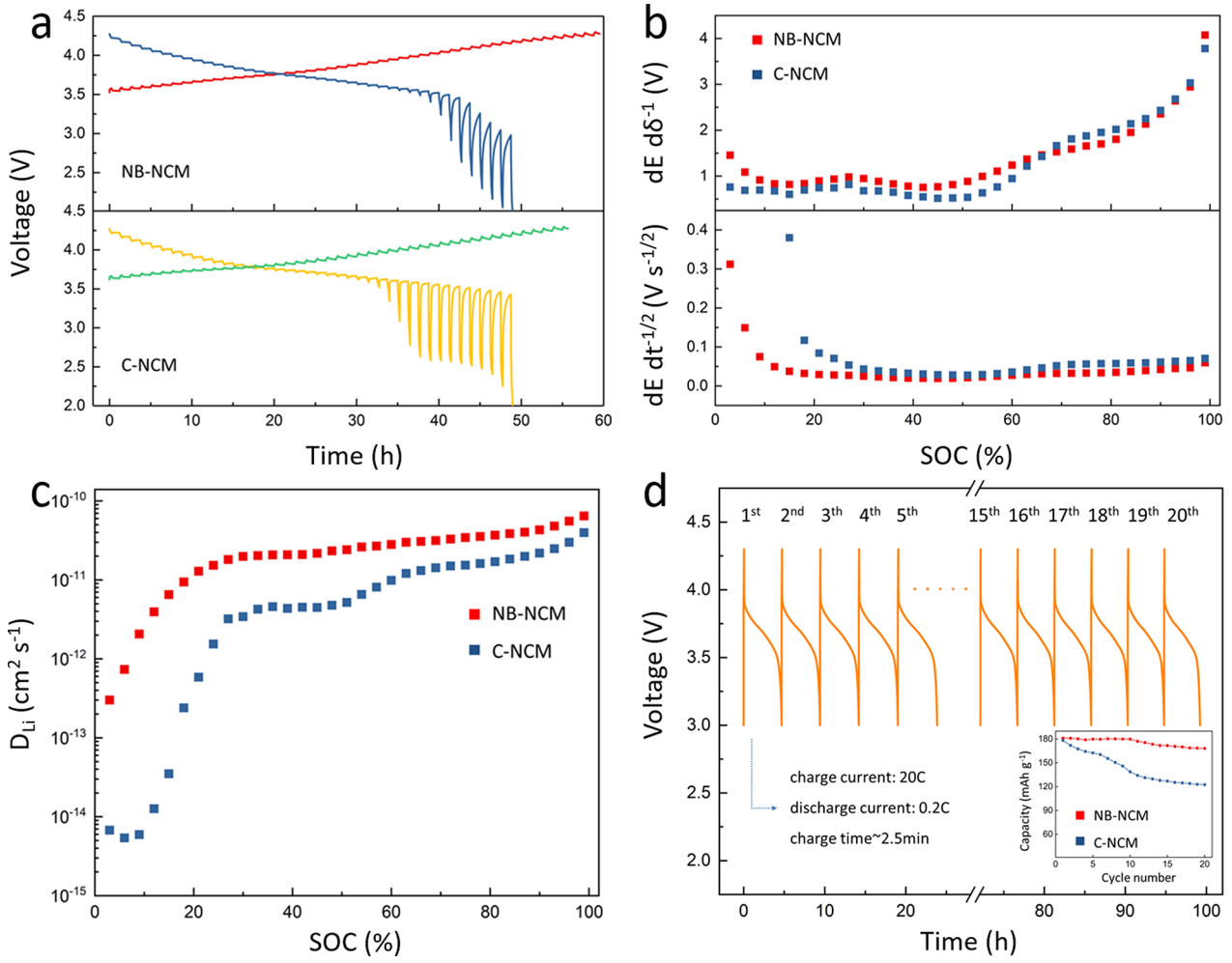

Figure 5. (a) GITT curves for both electrodes as a function of time. (b) $dE\ d\delta^{-1}$ and $dE\ dt^{-1/2}$ plots as a function of SOC. (c) Calculated D_{Li^+} values as a function of SOC. (d) Fast-charging capability of NB-NCM electrode (inset shows fast charging stability of both electrodes at 20 C rate).

These electrochemical results demonstrate that the as-prepared NB-NCM material is intrinsically superior with respect to both the cycle stability and rate capability, especially at high rates. On the one hand, the nanobrick electrode morphology will endure moderate stress during long-term cycling, thus providing improved stability. On the other hand, the structure with a high percentage of exposed {010} facets offers more Li-ion diffusion channels, which is beneficial for the fast (dis)charge performance.

Electrochemical impedance spectroscopy (EIS) has been performed with both electrodes to investigate the charge-transfer resistance in pristine and cycled electrodes (Figure 4c). Measurements are applied after every ten cycles for each battery. As shown in Figure S6, it is evident that NB-NCM reveals an ~4 times lower charge-transfer resistance in contrast to C-NCM during cycling. For instance, R_{ct} of NB-NCM is around 35 ohm after 100 cycles, while that of C-NCM is 137 ohm. The excellent charge-transfer kinetics of NB-NCM results from the modification of the surface chemistry, as demonstrated by XPS, and the ability to keep the structural stability upon electrochemical cycling.

To further explore the electrochemical behavior of both electrodes, the first two voltage charge−discharge curves are shown in Figure 4d (at 0.1 C in the voltage range of 3.0 to 4.3 V). Both NB-NCM and C-NCM deliver a comparable discharge capacity of 178.9 mAh g^{-1} and 177.3 mAh g^{-1}, respectively. C-NCM presents a sharp peak during the initial stages of the first charge cycle, which is related to Li_2CO_3 and Li(OH) residues at the Ni-rich electrode surface.[32] At the beginning of the first and second charge curves, the NB-NCM cathode displays a significantly lower voltages of around 50 mV compared to those of the C-NCM electrode (130 mV). This indicates that the deintercalation of Li ions from the NB-NCM electrode is indeed more facile. Cyclic voltammetry (CV) has also been performed to study the oxidation and reduction peaks of the electrode materials. As indicated in Figure 4e, both samples have a couple of oxidation and reduction peaks, which represent the delithiation and lithiation processes, respectively. Notably, in the second cycle, the separation between the oxidation and reduction peak is around 18 mV for the NB-NCM cathode, while the value for C-NCM is 55 mV. The substantially reduced voltage separation for NB-NCM demonstrates a decreased electrochemical polarization in contrast to the C-NCM cathode.[41] Corresponding differential capacity vs voltage (dQ/dV) curves obtained from Figure 4d are also provided in Figure 4f. The dQ/dV curves are in good agreement with the measured CV curves, except that the oxidation peak splits into two peaks, revealing the actual phase transitions of cathodes. During the first cycle both electrodes exhibit a sharp oxidation peak which is related to the activation

https://dx.doi.org/10.1021/acsaem.0c00765
ACS Appl. Energy Mater. 2020, 3, 6583−6590

process. After activation, two secondary oxidation peaks appear during the deintercalation process, denoted as peaks A and B. According to previous studies, peaks A and B have been identified as phase transition from hexagonal (H1) to monoclinic (M) and monoclinic (M) to hexagonal (H2).[42] In accordance with the CV curves of the second cycle, lower oxidation peaks and smaller voltage separation between the oxidation and reduction peaks are observed for the NB-NCM electrode.

GITT is a reliable method to evaluate the diffusion coefficient (D_{Li^+}) of lithium ions inside electrode materials. Figure 5a displays typical GITT curves for both electrodes as a function of time with an applied current of 0.02 C in the voltage range of 2.0−4.3 V. The D_{Li^+} values can be calculated according to eq 1, which has been derived from Fick's second law[43−45]

$$D_{Li^+} = \frac{4}{\pi}\left(\frac{V_M}{FS}\right)^2\left[I\left(\frac{dE}{d\delta}\right)/\left(\frac{dE}{d\sqrt{\tau}}\right)\right]^2 \quad \tau \ll L^2/D_{Li^+} \tag{1}$$

where V_M [$cm^3\ mol^{-1}$] is the molar volume of the electrode material, F [$C\ mol^{-1}$] the Faraday constant, S [cm^2] the area of the electrode−electrolyte interface, I [A] the applied current during the titration process, L [cm] the electrode thickness, E [V] the equilibrium voltage, and δ the stoichiometric index in $Li_\delta MeO_2$. In eq 1, two differential factors $dE/d\delta$ and $dE/d\sqrt{r}$ are the most crucial values in the calculations. Both derivatives are estimated by finite differences, e.g., $\frac{dE}{d\delta} \approx \frac{\Delta E}{\Delta\delta}$, where ΔE is the decrement of the equilibrium voltage during titration period and $\Delta\delta$ is the change of the electrode stoichiometry caused by coulometric titration. ΔE can be found from the voltages observed at the end of relaxation periods after each two subsequent titrations. $\Delta\delta$ obeys

$$\Delta\delta = \frac{I\tau M_B}{z m_B F} \tag{2}$$

where τ [s] is the time interval of the current titration, M_B [$g\ mol^{-1}$] the atomic weight of the electrode material, z [−] the valence number of Li ions, and m_B [g] the mass loading of active material in the electrode. Similarly $\frac{dE}{d\sqrt{\tau}} \approx \frac{\Delta E}{\Delta\sqrt{\tau}}$, where $\Delta\sqrt{r}$ is the increment of the square root of the current titration time. Both differential factors during the discharging process are shown in Figure 5b as a function of SOC for the two electrodes. The calculated values for D_{Li^+} are summarized in Figure 5c as a function of SOC. The NB-NCM electrode reveals D_{Li^+} values in the range from 3.0×10^{-13} to 6.45×10^{-11} $cm^2\ s^{-1}$, while those of C-NCM are significantly lower in the range of 6.74×10^{-15} to 3.96×10^{-11} $cm^2\ s^{-1}$. It can be concluded that the NB-NCM electrode clearly shows higher D_{Li^+} values compared to those of the C-NCM electrode.

The higher Li-ion diffusion coefficient is also in favor for the fast-charging performance of the NB-NCM electrode. As shown in Figure 5d, an ultrahigh charging current of 20 C and a relatively low discharging current (0.2 C) are applied to both electrodes to evaluate their fast-charging storage capacity. The charging time is estimated at around 2.5 min. The inset of Figure 5d shows a sharp distinction in extracted capacity between NB-NCM and C-NCM. NB-NCM still maintains 93.3% capacity after 20 cycles, while the performance of C-NCM deteriorates severely, and only 68.5% capacity remains after cycling. Another possible conclusion is These results in terms of high D_{Li^+} and excellent fast-charging ability of NB-NCM illustrate that a well-designed structure with the same orientation and high exposure of active {010} facets contributes to the enhanced electrochemical performance. This architecture can not only promote the Li^+ diffusion but also withstand the Li^+ intercalation and deintercalation behavior even at high current densities.

The electrodes after long-term cycling are disassembled and characterized by cross-sectional SEM. It has been reported that crack formation occurring inside the particles is the main reason leading to the capacity decay during cycling. Figure 6a,b shows the morphology of postcycled C-NCM and NB-NCM particles. The small residues attached at the particle surface are carbon black, used during the cathode slurry preparation. The cycled C-NCM has extensive cracks throughout the surface, as emphasized by the arrows, suggesting anisotropic volume expansion inside the particles during Li^+ insertion and extraction. On the other hand, the structure of the cycled NB-NCM particle remains intact and crack-free at the surface.

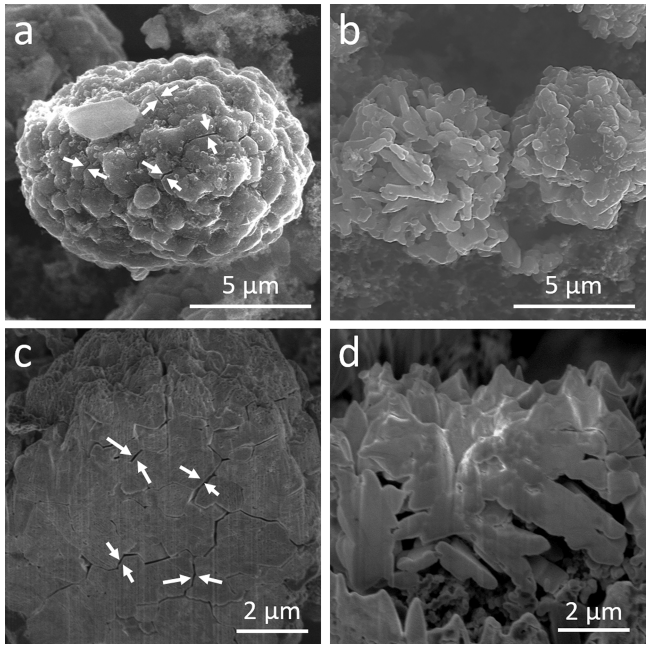

Figure 6. SEM images of (a) an C-NCM particle and (b) NB-NCM particle after cycling. SEM images of the cross section of (c) an C-NCM particle and (d) NB-NCM particle.

To study structural changes inside the particles after long-term cycling, randomly selected particles were selected and subjected to focused-ion beam (FIB) processing. Figure 6c shows further fracturing inside the C-NCM particle. Cracks inside the C-NCM particles result from internal grain stress induced by the anisotropic volume change during (dis)-charging. The as-formed cracks then block the electronic connection between the particles and consequently sacrificed parts of the active material. The electrolyte will also penetrate through the cracks and accelerate the formation of contaminating layers, such as Li_xCO_3 and LiOH, resulting in the observed capacity losses.[45] On the contrary, the NB-NCM electrode reveals a well-preserved intrinsic architecture over the same cycling period (Figure 6d and Figure S9) because of the ordered orientation of morphology and accordant volume change of each primary nanobrick. Besides, the unique

https://dx.doi.org/10.1021/acsaem.0c00765
ACS Appl. Energy Mater. 2020, 3, 6583−6590

structure with improved Li-ion diffusion coefficient is in favor of the homogeneous formation of the inevitable contaminating layer and contributing to the alleviated capacity decay during cycling.

4. CONCLUSIONS

In summary, Ni-rich $LiNi_{0.6}Co_{0.2}Mn_{0.2}O_2$ cathode materials with a well-structured nanobrick morphology have been developed by using a facile surfactant-assisted hydrothermal method followed by solid-state reaction. HRTEM and corresponding SAED analyses validate the crystal facet orientation of the nanobrick $LiNi_{0.6}Co_{0.2}Mn_{0.2}O_2$ cathode and show the exposed active {010} facets in the particles, which can facilitate the presence of Li-ion diffusion tunnels and improve the Li-ion diffusivity. Benefiting from the structural advantage, the nanobrick $LiNi_{0.6}Co_{0.2}Mn_{0.2}O_2$ cathode demonstrates a more favorable Li-ion (de)intercalation reaction kinetics, promising discharge rate capability and stable cycling performances compared with the commercial sample. Additionally, faster reaction kinetics also endowed the NB-NCM material the ability of the fast-charging property, showing the high potential for practical applications in the Li-ion batteries. However, it is noteworthy that the tap density for this nanostructured material has not been improved due to its porous structure. To further improve this as well as to maintain the exposure of high-energy facets, we do need to find more suitable pathways. One possible way would be to apply a modified coprecipitation method, carefully control the concentration of precipitant, and/or introduce new reagents and surfactant into the synthesis process.[27,41] In this way, we can ultimately facilitate the agglomeration of small secondary particles and improve the compactness of the materials.

■ ASSOCIATED CONTENT

Supporting Information

The Supporting Information is available free of charge at https://pubs.acs.org/doi/10.1021/acsaem.0c00765.

Additional figures including SEM, EDX, TEM, XRD, and additional electrochemical data (PDF)

■ AUTHOR INFORMATION

Corresponding Authors

Peter H. L. Notten − *Eindhoven University of Technology, 5600 MB Eindhoven, The Netherlands; IEK-9, Forschungszentrum Jülich, D-52425 Jülich, Germany; University of Technology Sydney, Broadway, Sydney NSW 2007, Australia;* orcid.org/0000-0003-4907-8426; Email: p.h.l.notten@tue.nl

Qian Zhang − *IEK-9, Forschungszentrum Jülich, D-52425 Jülich, Germany; RWTH Aachen University, D-52074 Aachen, Germany*; Email: qia.zhang@fz-juelich.de

Authors

Ming Jiang − *Eindhoven University of Technology, 5600 MB Eindhoven, The Netherlands; IEK-9, Forschungszentrum Jülich, D-52425 Jülich, Germany*

Xiaochao Wu − *IEK-9, Forschungszentrum Jülich, D-52425 Jülich, Germany; Polymer Technology Group Eindhoven (PTG/e) B.V., 5600 HG Eindhoven, The Netherlands*

Zhiqiang Chen − *Eindhoven University of Technology, 5600 MB Eindhoven, The Netherlands; IEK-9, Forschungszentrum Jülich, D-52425 Jülich, Germany*

Dmitri L. Danilov − *Eindhoven University of Technology, 5600 MB Eindhoven, The Netherlands; IEK-9, Forschungszentrum Jülich, D-52425 Jülich, Germany*

Rüdiger-A. Eichel − *IEK-9, Forschungszentrum Jülich, D-52425 Jülich, Germany; RWTH Aachen University, D-52074 Aachen, Germany*

Complete contact information is available at: https://pubs.acs.org/10.1021/acsaem.0c00765

Notes

The authors declare no competing financial interest.

■ ACKNOWLEDGMENTS

M.J. gratefully acknowledges a fellowship support by the China Scholarship Council. The authors also acknowledge Y. Zhang from the Eindhoven University of Technology for XPS measurements.

■ REFERENCES

(1) Cui, Q.; Zhong, Y.; Pan, L.; Zhang, H.; Yang, Y.; Liu, D.; Teng, F.; Bando, Y.; Yao, J.; Wang, X. Recent Advances in Designing High-Capacity Anode Nanomaterials for Li-Ion Batteries and Their Atomic-Scale Storage Mechanism Studies. *Adv. Sci.* **2018**, *5* (7), 1700902.

(2) Hapuarachchi, S. N. S.; Sun, Z.; Yan, C. Advances in In Situ Techniques for Characterization of Failure Mechanisms of Li-Ion Battery Anodes. *Adv. Sustain. Syst.* **2018**, *2* (8−9), 1700182.

(3) Schmuch, R.; Wagner, R.; Hörpel, G.; Placke, T.; Winter, M. Performance and cost of materials for lithium-based rechargeable automotive batteries. *Nat. Energy* **2018**, *3* (4), 267−278.

(4) Kim, T.-H.; Park, J.-S.; Chang, S. K.; Choi, S.; Ryu, J. H.; Song, H.-K. The Current Move of Lithium Ion Batteries Towards the Next Phase. *Adv. Energy Mater.* **2012**, *2* (7), 860−872.

(5) Goodenough, J. B. How we made the Li-ion rechargeable battery. *Nat. Electron.* **2018**, *1* (3), 204−204.

(6) Natarajan, S.; Aravindan, V. Burgeoning Prospects of Spent Lithium-Ion Batteries in Multifarious Applications. *Adv. Energy Mater.* **2018**, *8* (33), 1802303.

(7) Zuo, X.; Zhu, J.; Müller-Buschbaum, P.; Cheng, Y.-J. Silicon based lithium-ion battery anodes: A chronicle perspective review. *Nano Energy* **2017**, *31* (31), 113−143.

(8) Su, X.; Wu, Q.; Li, J.; Xiao, X.; Lott, A.; Lu, W.; Sheldon, B. W.; Wu, J. Silicon-Based Nanomaterials for Lithium-Ion Batteries: A Review. *Adv. Energy Mater.* **2014**, *4* (1), 1300882.

(9) Zhang, W.-J. A review of the electrochemical performance of alloy anodes for lithium-ion batteries. *J. Power Sources* **2011**, *196* (1), 13−24.

(10) Kasavajjula, U.; Wang, C.; Appleby, A. J. Nano- and bulk-silicon-based insertion anodes for lithium-ion secondary cells. *J. Power Sources* **2007**, *163* (2), 1003−1039.

(11) Schipper, F.; Erickson, E. M.; Erk, C.; Shin, J.-Y.; Chesneau, F. F.; Aurbach, D. Review—Recent Advances and Remaining Challenges for Lithium Ion Battery Cathodes. *J. Electrochem. Soc.* **2017**, *164* (1), A6220−A6228.

(12) Manthiram, A.; Song, B.; Li, W. A perspective on nickel-rich layered oxide cathodes for lithium-ion batteries. *Energy Stor. Mater.* **2017**, *6*, 125−139.

(13) Cui, S.; Wei, Y.; Liu, T.; Deng, W.; Hu, Z.; Su, Y.; Li, H.; Li, M.; Guo, H.; Duan, Y.; Wang, W.; Rao, M.; Zheng, J.; Wang, X.; Pan, F. Optimized Temperature Effect of Li-Ion Diffusion with Layer Distance in $Li(Ni_xMn_yCo_z)O_2$ Cathode Materials for High Performance Li-Ion Battery. *Adv. Energy Mater.* **2016**, *6* (4), 1501309.

(14) Chen, Z.; Kim, G.-T.; Guang, Y.; Bresser, D.; Diemant, T.; Huang, Y.; Copley, M.; Behm, R. J.; Passerini, S.; Shen, Z. Manganese phosphate coated $Li[Ni_{0.6}Co_{0.2}Mn_{0.2}]O_2$ cathode material: Towards superior cycling stability at elevated temperature and high voltage. *J. Power Sources* **2018**, *402*, 263−271.

(15) Liu, W.; Li, X.; Xiong, D.; Hao, Y.; Li, J.; Kou, H.; Yan, B.; Li, D.; Lu, S.; Koo, A.; Adair, K.; Sun, X. Significantly improving cycling performance of cathodes in lithium ion batteries: The effect of Al_2O_3 and $LiAlO_2$ coatings on $LiNi_{0.6}Co_{0.2}Mn_{0.2}O_2$. *Nano Energy* **2018**, *44*, 111−120.
(16) Zhao, J.; Zhang, W.; Huq, A.; Misture, S. T.; Zhang, B.; Guo, S.; Wu, L.; Zhu, Y.; Chen, Z.; Amine, K.; Pan, F.; Bai, J.; Wang, F. In Situ Probing and Synthetic Control of Cationic Ordering in Ni-Rich Layered Oxide Cathodes. *Adv. Energy Mater.* **2017**, *7* (3), 1601266.
(17) Ryu, H.-H.; Park, K.-J.; Yoon, C. S.; Sun, Y.-K. Capacity Fading of Ni-Rich $Li[Ni_xCo_yMn_{1-x-y}]O_2$ ($0.6 \leq x \leq 0.95$) Cathodes for High-Energy-Density Lithium-Ion Batteries: Bulk or Surface Degradation? *Chem. Mater.* **2018**, *30* (3), 1155−1163.
(18) Sun, H.-H.; Manthiram, A. Impact of Microcrack Generation and Surface Degradation on a Nickel-Rich Layered $Li[Ni_{0.9}Co_{0.05}Mn_{0.05}]O_2$ Cathode for Lithium-Ion Batteries. *Chem. Mater.* **2017**, *29* (19), 8486−8493.
(19) Gao, S.; Zhan, X.; Cheng, Y.-T. Structural, electrochemical and Li-ion transport properties of Zr-modified $LiNi_{0.8}Co_{0.1}Mn_{0.1}O_2$ positive electrode materials for Li-ion batteries. *J. Power Sources* **2019**, *410*−*411*, 45−52.
(20) Ran, Q.; Zhao, H.; Shu, X.; Hu, Y.; Hao, S.; Shen, Q.; Liu, W.; Liu, J.; Zhang, M.; Li, H.; Liu, X. Enhancing the Electrochemical Performance of Ni-Rich Layered Oxide Cathodes by Combination of the Gradient Doping and Dual-Conductive Layers Coating. *ACS Appl. Energy Mater.* **2019**, *2* (5), 3120−3130.
(21) Jo, C.-H.; Cho, D.-H.; Noh, H.-J.; Yashiro, H.; Sun, Y.-K.; Myung, S. T. An effective method to reduce residual lithium compounds on Ni-rich $Li[Ni_{0.6}Co_{0.2}Mn_{0.2}]O_2$ active material using a phosphoric acid derived Li_3PO_4 nanolayer. *Nano Res.* **2015**, *8* (5), 1464−1479.
(22) Jo, C.-H.; Cho, D.-H.; Lee, J.-w.; Hitoshi, Y.; Myung, S.-T. Surface coating effect on thermal properties of delithiated lithium nickel manganese layer oxide. *J. Power Sources* **2015**, *282*, 511−519.
(23) Kim, H.; Kim, M. G.; Jeong, H. Y.; Nam, H.; Cho, J. A new coating method for alleviating surface degradation of $LiNi_{0.6}Co_{0.2}Mn_{0.2}O_2$ cathode material: nanoscale surface treatment of primary particles. *Nano Lett.* **2015**, *15* (3), 2111−9.
(24) Chen, Y.; Li, P.; Li, Y.; Su, Q.; Xue, L.; Han, Q.; Cao, G.; Li, J. Enhancing the high-voltage electrochemical performance of the $LiNi_{0.5}Co_{0.2}Mn_{0.3}O_2$ cathode materials via hydrothermal lithiation. *J. Mater. Sci.* **2018**, *53* (3), 2115−2126.
(25) Tang, Z.-F.; Wu, R.; Huang, P.-F.; Wang, Q.-S.; Chen, C.-H. Improving the electrochemical performance of Ni-rich cathode material $LiNi_{0.815}Co_{0.15}Al_{0.035}O_2$ by removing the lithium residues and forming Li_3PO_4 coating layer. *J. Alloys Compd.* **2017**, *693*, 1157−1163.
(26) Wei, G. Z.; Lu, X.; Ke, F. S.; Huang, L.; Li, J. T.; Wang, Z. X.; Zhou, Z. Y.; Sun, S. G. Crystal habit-tuned nanoplate material of $Li[Li_{1/3-2x/3}Ni_xMn_{2/3-x/3}]O_2$ for high-rate performance lithium-ion batteries. *Adv. Mater.* **2010**, *22* (39), 4364−7.
(27) Zhang, L.; Li, N.; Wu, B.; Xu, H.; Wang, L.; Yang, X. Q.; Wu, F. Sphere-shaped hierarchical cathode with enhanced growth of nanocrystal planes for high-rate and cycling-stable li-ion batteries. *Nano Lett.* **2015**, *15* (1), 656−61.
(28) Xu, M.; Fei, L.; Zhang, W.; Li, T.; Lu, W.; Zhang, N.; Lai, Y.; Zhang, Z.; Fang, J.; Zhang, K.; Li, J.; Huang, H. Tailoring Anisotropic Li-Ion Transport Tunnels on Orthogonally Arranged Li-Rich Layered Oxide Nanoplates Toward High-Performance Li-Ion Batteries. *Nano Lett.* **2017**, *17* (3), 1670−1677.
(29) Cho, Y.; Oh, P.; Cho, J. A new type of protective surface layer for high-capacity Ni-based cathode materials: nanoscaled surface pillaring layer. *Nano Lett.* **2013**, *13* (3), 1145−52.
(30) Fu, F.; Xu, G.-L.; Wang, Q.; Deng, Y.-P.; Li, X.; Li, J.-T.; Huang, L.; Sun, S.-G. Synthesis of single crystalline hexagonal nanobricks of $LiNi_{1/3}Co_{1/3}Mn_{1/3}O_2$ with high percentage of exposed {010} active facets as high rate performance cathode material for lithium-ion battery. *J. Mater. Chem. A* **2013**, *1* (12), 3860−3864.
(31) Tian, J.; Su, Y.; Wu, F.; Xu, S.; Chen, F.; Chen, R.; Li, Q.; Li, J.; Sun, F.; Chen, S. High-Rate and Cycling-Stable Nickel-Rich Cathode Materials with Enhanced Li(+) Diffusion Pathway. *ACS Appl. Mater. Interfaces* **2016**, *8* (1), 582−7.
(32) Ju, X.; Huang, H.; He, W.; Zheng, H.; Deng, P.; Li, S.; Qu, B.; Wang, T. Surfactant-Assisted Synthesis of High Energy {010} Facets Beneficial to Li-Ion Transport Kinetics with Layered $LiNi_{0.6}Co_{0.2}Mn_{0.2}O_2$. *ACS Sustainable Chem. Eng.* **2018**, *6* (5), 6312−6320.
(33) Xiang, W.; Liu, W.-Y.; Zhang, J.; Wang, S.; Zhang, T.-T.; Yin, K.; Peng, X.; Jiang, Y.-C.; Liu, K.-H.; Guo, X.-D. Controlled synthesis of nickel-rich layered oxide cathodes with preferentially exposed {010} active facets for high rate and long cycling stable lithium-ion batteries. *J. Alloys Compd.* **2019**, *775*, 72−80.
(34) Ma, Y.; Zhang, C.; Hou, C.; Zhang, H.; Zhang, H.; Zhang, Q.; Guo, Z. Cetyl trimethyl ammonium bromide (CTAB) micellar templates directed synthesis of water-dispersible polyaniline rhombic plates with excellent processability and flow-induced color variation. *Polymer* **2017**, *117*, 30−36.
(35) Fu, J.; Mu, D.; Wu, B.; Bi, J.; Cui, H.; Yang, H.; Wu, H.; Wu, F. Electrochemical Properties of the $LiNi_{0.6}Co_{0.2}Mn_{0.2}O_2$ Cathode Material Modified by Lithium Tungstate under High Voltage. *ACS Appl. Mater. Interfaces* **2018**, *10* (23), 19704−19711.
(36) Phillip, N. D.; Ruther, R. E.; Sang, X.; Wang, Y.; Unocic, R. R.; Westover, A. S.; Daniel, C.; Veith, G. M. Synthesis of Ni-Rich Thin-Film Cathode as Model System for Lithium Ion Batteries. *ACS Applied Energy Materials* **2019**, *2* (2), 1405−1412.
(37) Zhang, Y.; Wang, Z.-B.; Yu, F.-D.; Que, L.-F.; Wang, M.-J.; Xia, Y.-F.; Xue, Y.; Wu, J. Studies on stability and capacity for long-life cycle performance of $Li(Ni_{0.5}Co_{0.2}Mn_{0.3})O_2$ by Mo modification for lithium-ion battery. *J. Power Sources* **2017**, *358*, 1−12.
(38) Ran, Q.; Zhao, H.; Wang, Q.; Shu, X.; Hu, Y.; Hao, S.; Wang, M.; Liu, J.; Zhang, M.; Li, H.; Liu, N.; Liu, X. Dual functions of gradient phosphate polyanion doping on improving the electrochemical performance of Ni-rich $LiNi_{0.6}Co_{0.2}Mn_{0.2}O_2$ cathode at high cut-off voltage and high temperature. *Electrochim. Acta* **2019**, *299*, 971−978.
(39) Shi, Y.; Zhang, M.; Fang, C.; Meng, Y. S. Urea-based hydrothermal synthesis of $LiNi_{0.5}Co_{0.2}Mn_{0.3}O_2$ cathode material for Li-ion battery. *J. Power Sources* **2018**, *394*, 114−121.
(40) Xu, X.; Huo, H.; Jian, J.; Wang, L.; Zhu, H.; Xu, S.; He, X.; Yin, G.; Du, C.; Sun, X. Radially Oriented Single-Crystal Primary Nanosheets Enable Ultrahigh Rate and Cycling Properties of $LiNi_{0.8}Co_{0.1}Mn_{0.1}O_2$ Cathode Material for Lithium-Ion Batteries. *Adv. Energy Mater.* **2019**, *9* (15), 1803963.
(41) Woo, S.-U.; Yoon, C. S.; Amine, K.; Belharouak, I.; Sun, Y.-K. Significant improvement of electrochemical performance of AlF_3-coated $Li[Ni_{0.8}Co_{0.1}Mn_{0.1}]O_2$ cathode materials. *J. Electrochem. Soc.* **2007**, *154* (11), A1005−A1009.
(42) Shen, Z.; Cao, L.; Rahn, C. D.; Wang, C.-Y. Least Squares Galvanostatic Intermittent Titration Technique (LS-GITT) for Accurate Solid Phase Diffusivity Measurement. *J. Electrochem. Soc.* **2013**, *160* (10), A1842−A1846.
(43) Yu, R.; Wang, X.; Wang, D.; Ge, L.; Shu, H.; Yang, X. Self-assembly synthesis and electrochemical performance of $Li_{1.5}Mn_{0.75}Ni_{0.15}Co_{0.10}O_{2+\delta}$ microspheres with multilayer shells. *J. Mater. Chem. A* **2015**, *3* (6), 3120−3129.
(44) Weppner, W.; Huggins, R. A. Determination of the kinetic parameters of mixed-conducting electrodes and application to the system Li_3Sb. *J. Electrochem. Soc.* **1977**, *124* (10), 1569−1578.
(45) Liu, W.; Oh, P.; Liu, X.; Lee, M. J.; Cho, W.; Chae, S.; Kim, Y.; Cho, J. Nickel-rich layered lithium transition-metal oxide for high-energy lithium-ion batteries. *Angew. Chem., Int. Ed.* **2015**, *54* (15), 4440−57.

https://dx.doi.org/10.1021/acsaem.0c00765
ACS Appl. Energy Mater. 2020, 3, 6583−6590